Desalination and Water Treatment
www.deswater.com

doi: 10.1080/19443994.2015.1119736

57 (2016) 21211–21233
September

Taylor & Francis
Taylor & Francis Group

Numerical investigations: basin materials of a single-basin and single-slope solar still

Prakash Malaiyappan*, Natarajan Elumalai

Institute for Energy Studies, CEG, Anna University, Chennai 600025, India, Tel. +91 9444709357; email: prakashmalaiyapan@gmail.com (P. Malaiyappan), Tel. +91 2235 7603; Fax: +91 2235 3637; email: enat123@annauniv.edu (N. Elumalai)

Received 8 February 2015; Accepted 4 November 2015

ABSTRACT

Numerical computations were carried out for the experiments conducted with three different still materials. The phase change interactions were captured between the water evaporating into vapour at the liquid–vapour interface and the condensing vapour into water droplets at the top glass surface. The objective of the present CFD analysis was to validate the computational methodology adopted presently and to understand the system characteristics in detail, which would otherwise be difficult to estimate experimentally. The results from the computations are presented here in this work and the total quantity of freshwater condensed i.e. the productivity of the still was compared with the corresponding experiments.

Keywords: Solar stills; CFD; Evaporation; Condensation; Productivity; Basin materials; Feed water system; Performance; Desalination; Solar radiation; Solar energy

1. Introduction

Solar still represents one of the ancient models for the production of freshwater from unpalatable water, viz brackish water, saline water, brine water and sea water [1,2]. Double-basin still has the highest distillate productivity compared with single-basin still by 85% for the same basin condition and minor deviation below 10% between theoretical and experimental results [3]. The hybrid photovoltaic thermal (PVT) double-slope active solar still has the distillate productivity 1.4 times higher than the single-slope hybrid (PVT) active solar still [4]. A single-basin and single-slope solar still coupled with the helical copper wire, aluminium fins and stainless steel tube increase the distillate productivity by 92% [5]. The single-basin solar still with black sand beds increases productivity more than 50% [6]. The fin-type solar still with the industrial effluents, sponges, pebbles, black rubber and sand combination has 75% increase in productivity [7]. The single-basin double-slope solar still with the quartzite rock in the basin has a water temperature of 60˚C in the morning and it continuously decreases in the evening [8]. The solar still with an integrated flat-plate collector and conventional basin stills has the maximum productivity of 0.58 and 0.42 kg/m^2, respectively, which are obtained with 1-cm depth at 2.00 PM, 23 March 2013 in Madurai, Tamil Nadu, India. Double-slope passive and active solar still have the productivity under natural mode of 1.838 and 2.791 kg/m^2, respectively [9]. The thermal efficiency of the system is paramount than the exergy efficiency. The

*Corresponding author.

instantaneous thermal efficiency of solar still varies between 0 and 23.9% and is greater than the thermal efficiency of active solar still which is 0–17.9%. The instantaneous thermal efficiency and the instantaneous exergy efficiency for active solar still are paramount between 0 and 1.958% as compared to the exergy efficiency of solar still varying between 0 and 2.245% [10].

Air-blown heat recycling solar still has the steady-state productivity of 1 $kg/m^2/h$ by varying the gas flow rate between 1.5 and 4 m^3/m^2 h and the feedstock flow rate between 2 and 4 $kg/m^2/h$, respectively [11]. The solar still productivity is enhanced by a radiative cooling and packed bed storage tank (external condenser), which are cooled during the night using pure water into both [12]. Multiple-effect solar still has the overall distillation rate of the still which is 0.364 g m^2/h under solar radiation of 500 W/m^2 and the 22 MJ m^2/d overall daily solar radiation. The daily productivity is calculated to be 16 $kg/m^2/d$ from a multiple of 0.364 g m^{-2} s^{-1} and 22 MJ $L/m^2/d$, divided by 500 W/m^2 solar radiation [13]. The inverted V-type solar still has the low productivity of 13–17% without insulation. The soot with 2.5-cm thickness covers the system and has the productivity of 2–4 $l/m^2/d$. A land area for active stills of 20 000 m^2, 32 modules, each of 625 m^2 area (50 × 12.5 m), the yearly expense for an 8% fixed charge rate is 2–42 $\$/m^3$ and the yearly expense operation cost is 0.9 US$/$m^3$ without taxes [14]. A solar still with polyvinyl chloride tubes has the low thermal conductivity, high coefficient of thermal expansion and also the price for the small and large thickness is 3.00 and 8.00 €/m, respectively, for desalting the sea water [15]. A flower pot transparent cap solar still manufacturing cost about $20/$m^2$ with lifetime of one thousand days, the distillate cost was estimated around $7/$m^3$ at 3 $L/m^2/d$ [16]. A solar still made of fibre–cement (corrosion-proof materials) with two concentric commercial-type cylindrical chambers integrated with a solar pond has a productivity of 40 L/d with the maximum temperature of 65°C [17]. Compound parabolic concentrator concentric tubular solar still (CPC-CTSS) has the yield increased by 49%–3.05 L/d with cooling air flow effect and with cooling water flow, the yield further increased by 64% compared with the air flow. The CTSS with cold water flow has the highest productivity of 144% with respect to the ordinary CPC-CTSS without air or water flow [18]. The cascade solar still had the highest colonies forming units of 1,400 CFU/ml, compared to the electrically powered still of 22 CFU/ml, and tap water of 12 CFU/ml. The selected parameters (concentrations) of iron (0.875), lead (0.214), calcium (2.060), zinc (1.443), sodium (2.109), pH (0.218), conductivity (1.888), turbidity (0.436), total suspended solids (1.081), chloride ions (1.081) and microbiological assays (0.939) [19]. A single-stage basin-type solar still has the daily yield of 2 $L/m^2/d$ with daily efficiency of 27%. The system (solar still) is integrated with the conventional flat-plate collector for 24 h which has the yield of 231% but efficiency decreases by 2.5%. The system with same collector operating from 8 am to 5 pm has the yield of 4.687 L and efficiency of 25.8% [20].

A plastic solar still with two basins superimposed upon each other in order to utilize the waste latent heat accumulated between the water layer and glass layer. This arrangement increases the distillation productivity by 5–5.5 $L/m^2/d$ [21]. The hybrid active solar still has the thermal efficiency of 20% higher than the normal solar still. The daily productivity of the hybrid active solar still in summer and winter month is 3.2 and 5.5 times, respectively, higher than the normal solar still [22]. "V"-type solar still with a charcoal absorber has 30.05% of overall efficiency with the centre collection of the productivity. The experimental value for the density of water still without boosting mirror is 1.1499–1.0797 kg m^{-3}, with the boosting mirror 1.1555–1.0492 kg m^{-3}, with floating charcoal without the boosting mirror 1.1499–1.06185 kg m^{-3} and with floating charcoal without the boosting mirror is 1.1555–1.0263 kg m^{-3} [23]. Pyramid-shaped solar still with the free and forced convection has the distillation yield around 2.99 and 2.485 L/d, respectively. The hourly variation of the still efficiency with the free and forced convection is 40.2 and 50.5%, respectively [24]. A tube-type solar still with wax has the productivity of 15%/d higher than without wax. For the highest irradiation intensity, 720 $g/m^2/h$ is the maximum error for the distillation rate per hour [25]. A double-slope solar still with sea water has the experimental and theoretical value global losses factor (U_L) of 2.76 W/m^2°C and (U_L) of 5.12 W/m^2°C, respectively [26]. The cost of the system (algal pond to co-treat solar still brine and sewage) for the freshwater productivity in Kaudikasa village is USD 20,418 [27]. The laboratory solar still for the distillate chemical oxygen demands for the first 3 d has no change. The contamination starts on day 4, the COD value is twice and on day 5 a high value of 566 mg/l is obtained [28]. A "V"-type solar still with and without cotton gauze top cover cooling has the yield of 3.3 and 4.3 $L/m^2/d$, respectively [29]. The parabolic-type solar still with a line concentrator has the maximum distillate for a period of four hours with average value of 0.16 $kg/m^2/h$ [30].

The solar still with and without solar dish concentrator has the daily average efficiency for brackish water desalination which is 68 and 34%, respectively.

The single-basin still has distillate production without and with preheating which is 244 and 347%, respectively [31]. A portable thermal–electrical solar still integrated with an external reflecting booster and outside condenser increases to 85% efficiency in continuous mode of operation by preheating saline water [32]. The single-basin solar still has the daily yield of 4.736 kg/m^2/d and daily efficiency of 39.6%. The still is modified with baffle-suspended absorber which has the daily yield of 5.737 kg/m^2/d of 47.8 and daily efficiency of 39.6% [33]. The inverted absorber solar still (IASS) with the curved reflector has a distillate productivity of 4 kg/m^2 for the water depth of 0.01 m and the annual cost of distilled water per kg/m^2 is Rs. 0.95/- [34]. Wind turbine-inclined still tests are made under these conditions: water depths of 0.01, 0.02, and 0.03 m, different water flow rates of 25.0, 41.7, and 58.3 ml/min and the modes of operation which are south facing having the efficiencies of 67.21–69.59 and 57.77–62.01% and the sun tracking having the efficiencies of 66.81–69.01 and 57.08–62.38%, respectively [35]. A stepped solar still of flashing chamber has the yield of 2.27 L/d/h under the following conditions, electric motor speed of 250 rpm, mass flow rate of 9.333 l/h, power consumption of 2.92 kW, base temperature of 76.7˚C, inner cover temperature of 53.6˚C, outer cover temperature of 38.9˚C, inlet water temperature of 28.7˚C, ambient air temperature of 32.3˚C and wind speed of 0.9 m/s [36]. The solar still with the sun tracking system has the increase in the yield around 22% compared to that without the sun tracking [37]. The theoretical results of solar still for 10 partitions with 5- or 3-mm diffusion gaps are 19.2 or 21.8 kg/m^2/d, respectively [38]. The single-effect device with the heating power source of 300 and 400 W has the maximum distillate productivity under steady-state conditions which is 0.445 and 0.495 kg/h, respectively. The single-effect device has the highest productivity compared with the two- and three-effect device under the same input power condition [39]. The dome-shaped solar still with a corresponding performance conversion ratio of 50% has the daily average efficiency of 33% [40].

Solar still with 5-mm diffusion gaps has the efficiency of 3.5 and 1.2–1.6 times higher than the average experimental results of the conventional basin-type stills and the multiple-effect stills, respectively [41]. The cost of freshwater for the vinyl chloride sheet and the polythene film tubular solar still cover model is 9,705 and 1,244 Yen/m^3 [42]. The inverted trickle solar still simulation result (steady state) shows 35–40% higher than the experimental result and the productivity increased from 2.5 to 2.8 L/d with the use of the brackish water [43]. The single-sloped solar still with the 3-cm water depth has a minor deviation of 4% for floating plate, 6% for plain water between the theoretical and experimental results [44]. The non-conventional solar stills with the charcoal particles act as both heat absorber and wick medium which supports the high flow rates and efficient removal of pollutants from the wastewater [45]. A novel continuous single-stage solar still with the phase change energy storage mixture (paraffin wax, paraffin oil and water) has the efficiency of 36.2% for the saline water flow rate which was 40 ml/min [46]. The solar still coupled with the evacuated tube collector has 107% increase in productivity compared with the solar still alone [47]. The comparison of the different basin materials integrated with solar stills is shown in Table 1.

2. Experimental set-up

Experimental set-up is a do-it-yourself device which consists of the container (basin material), the plastic storage tank, flexible hole and valve. The unpalatable water from the overhead supply tank is allowed to flow through the container of the solar still [1]. A sump is made to adjust the water level within an accuracy of 2 cm: the float actuates a valve (v1) connected to an overhead supply tank. The arrangements are made in such a way that the sun rays fall on the unpalatable water and reach the tray through the transparent medium (glass) which supports the film condensation for high efficiency. The condensing surface in the still is simply a 1.1 × 1.1 m^2 sloping glass cover [5]. The unpalatable water in the basin gets heated and due to this effect, a phase change occurs. The water vapour then rises and comes into contact with the transparent roof-shaped surface. In this surface, vapour further goes through a phase change from vapour back to liquid. This liquid runs off through the transparent inclined surface into a collection channel, which is made of plastic (prevent corrosion and rust) and connected to the measuring jar [5]. Fig. 1 skeleton shows basic working operation (evaporation, condensation and distillate productivity) in a single-basin and single-slope solar still. The optimum tilt angle of condensing cover for the test area Chennai, Tamil Nadu, India is 13˚, is taken from Table 2 [5]. The increase or decrease in the tilt angle results in decrease in the distillate productivity [5]. The condensing cover faced south direction, during all the experiments, in order to receive the maximum solar radiation. The experiments were conducted at Chennai from 8.30 AM to 8.30 PM, the following day during March 2014. The whole experimental set-up is kept in the south direction to receive the maximum solar radiation throughout the year.

Table 1
Comparison of different basin materials integrated with the solar still

S. No.	Technique	Key specification	Refs.	Integrating basin material	Results of yield
1	Single-basin solar still	Basin area = 250 mm Slope = 13˚ Glass cover = 5-mm thick	[1]	Sea water depth (4, 6, 8, 10, 12, 14, and 16 cm)	(1.2, 1.1, 1.05, 0.9, 0.85, 0.7, and 0.65 l/m^2/d)
2	Wick-type solar still	Basin area = 0.5 m^2, Slope = 30˚, glass sheet = 4-mm thick	[2]	Solar water heater system	114% increase in productivity
3	Double-basin still	Basin area = 0.9 m × 0.7 m × 0.008 m, slope = 30˚	[3]	Normal	2.99 l/d (4.75 l/m^2 d)
4	Single-basin double-slope active solar still	Basin area = 2.0 m × 1.0 m, slope = 15˚	[4]	Photovoltaic thermal (PVT)	7.54 kg/d
5	Single-basin solar still	Basin area = 1 m^2, slope = 13˚	[5]	Helical copper coil	1.79 kg/m^2 d
6	Solar Still	Basin area = 0.5 m^2 (0.5 m × 1 m), slope = 30˚	[6]	Sand	17–42% increase in productivity
7	Fin-type solar still	Basin area = 1 m^2, slope = 30˚	[7]	Sand and sponge combination	74% increase in productivity
8	Single-basin double-slope solar still	Inner basin size 2.08 m × 0.84 m × 0.075 m, outer basin size 2.3 m × 1 m × 0.25 m	[8]	Quartzite rock	3.66 l/d
9	Solar still	Basin area = 1 m^2, tilt angle = 10˚	[9]	Flat-plate collector	60% increase in production
10	Double-slope active solar still	Basin area = 1 m^2, slope = 15˚, glass cover = 4-mm thick	[10]	0.03 m water depth	51% increase in production
11	Laboratory-scale solar still	Basin area = 1,850 × 540 × 25 mm^3, slope = 20˚, glass cover = 4-mm thick	[11]	Feedstock flow rate of 6 kg m^{-2} h^{-1}	6–10% decrease in productivity
12	Basin type	Square basin area	[12]	Packed bed storage tank and radiative cooling panel	Improvement in the still performance
13	Multiple-effect solar still	Area = 1 m^2	[13]	Extended wicks on a sunny day	15 kg freshwater of 22 m^{-2} d^{-1}
14	Non symmetrical solar still	Basin area = 1 × 0.5 m^2, slope = 13˚, insulation thickness = 4 cm	[14]	Soot layer (1) ≥ 560 W/m ^{2} (2) low range flux	(1) 35% increase in production (2) 50% increase in production
15	Solar still	Basin area = (width ~0.5 m; length ~2.0 m) m^2	[15]	Transparent plastic tubes	Increase in production considerably without tubes failure risks
16	Solar still	Basin area = 1 m^2, Net solar radiation 26.27 MJ m^{-2} d^{-1}	[16]	Polypropylene tray and polyethylene wrapping sheets	(1) Measured 3.54 kg

(*Continued*)

Table 1 (*Continued*)

S. No.	Technique	Key specification	Refs.	Integrating basin material	Results of yield
					(2) Calculated 2.35 kg 2 h from that of beam strength
17	Single-effect basin type	Cylindrical area = 1 m^3, (height of 1.2 m and a diameter of 1.1 m, insulation (Armstrong) = 13-mm thick	[17]	Spray evaporation	35% operating efficiency with 5 1/m^2 d for a correct insolation
18	Solar water desalting system	Basin area = 2 m	[18]	(1) without cooling	(1) 2,050 ml/d
				(2) with cooling	(2) 5,000 ml/d
19	Solar still	Basin area = 59´´ × 37´´ Slope = 10–15˚	[19]	(1) the cascade solar still	Water quality indices (WQI) (1) 4.50
				(2)the electrically powered still	(2) 3.76
				(3) tap water	(3) 29.35
20	Single-basin solar still	Basin area = 1 m^2, glass sheet = 0.003-m thick	[20]	35,000 of saline water with collector	52% increase in production
21	Solar still	Basin area = 0.165 m^2	[21]	Steady-state condition	0.065 kg MJ^{-1}
22	Solar still	Basin area = 1 m × 1 m	[22]	(1) Normal	(1) 2.26 kg for 0.05-m water depth
		Slope = 30˚		(2) Hybrid active solar still	(2) 7.22 kg 0.05-m water depth
23	"V" type	Basin area = 0.50 m × 0.50 m × 0.15 m, inward slope = 22˚	[23]	(1) Without charcoal	(1) 24.47% overall efficiency
				(2) With boosting mirror	(2) 11.92% overall efficiency
				(3) With boosting mirror and charcoal	(3) 14.11% overall efficiency
24	Pyramid-shaped solar still	Basin area = 0.95 m^2	[24]	Fan work with photovoltaic solar panels	25% increase in productivity
25	Tube-type solar still	Pyrex glass tube = (100 mm in outer diameter and 2.4 mm in thickness) half-cut outer tube(insulator) = inner diameter 100 mm, length 1,100 and 7 mm in thickness	[25]	The heat accumulator 7 polyethylene tubes (6 mm in inner diameter) filled wax	294.3 g/m^2
26	Double-slope plane solar still	Basin area = 1.39 m^2	[26]	Sea water (salinity of 37, 7 g/L)	4 L/m^2/d
		Slope = 23˚			
		Glass sheet = 1.1 × 1.1-m^2 mm thick			
27	Single-slope single-basin-type solar still	Basin area = 1 m^2	[27]	Hand pump Under groundwater	3 l/m^2/d
		Slope = 8.6˚			

(*Continued*)

Table 1 (*Continued*)

S. No.	Technique	Key specification	Refs.	Integrating basin material	Results of yield
28	Laboratory solar still	Basin area = 0.325 m^2	[28]	Chemical oxygen demand	
		Slope = 30°, glass sheet = 0.003-m thickness		(1) First days (2) On day 2 (3) On day 3 (4) The last day	(1) High value (2) Fairly stable (3) Increase of 35% (4) Increase of 102%
29	"V" type	Basin area = 2 m × 0.75 m × 0.05 m Slope = 2°	[29]	Cotton gauze top cover cooling and air	4,600 ml
30	Parabolic reflector type	Length of the parabolic reflector = 1.4 m, acceptance angle = 1°	[30]	Sea water	The experimental collector efficiency is 22.8% The theoretical collector efficiency is 22.3%
31	Solar still	Basin area = 0.5 m^2 (0.5 m × 1 m)	[31]	(1) The automatic tracking system, new boiler design (2) Nil	(1) 6.7 l/m^2/d (2) 1.5 l/0.5 m^2/d
32	Thermal–electrical solar still	Basin area = 1.0 m^2	[32]	External reflecting booster and an outside condenser	77% efficiency
33	Single-basin solar still	Basin area = 1.0 m^2 Slope = 15°	[33]	Baffle-suspended absorber	20% increase in productivity
34	Solar still	Basin area = 1 × 1 m^2, inclination angle = 23°	[34]	Normal	2.5 kg
35	Main solar still	Basin area = 1 m^2	[35]	Wind turbine (1) south (2) sun tracking	(1) 26.55 to 29.17% increase in productivity (2) 27.1 to 32.93% increase in productivity 54.48 l/m^2 d productivity 0.50026 thermal efficiency
36	Stepped solar still	Basin area = 1.54 × 0.65 m^2	[36]	Flash evaporation system	54.48 l/m^2 d productivity 0.50026 thermal efficiency
37	Solar still	Basin area = 1 m^2, slope = 32°, glass sheet = 16-mm thick	[37]	Sun tracking	2% increase in overall efficiency
38	Vertical multiple-effect still	Basin area = 1 m^2, slope = 45°, glass sheet = 5-mm thick	[38]	Heat-pipe solar collector	13% increase in productivity
39	Solar desalination devices	(1) Single-effect (evaporation area = 0.209 m^2) (2) Two-effect (evaporation area = 0.19 m^2 and 0.242 m^2) (3) Three-effect	[39]	Multi-effect tubular shell with the fixed heating power =300 W	20.08 kg/(m^2 d)

(*Continued*)

Table 1 (*Continued*)

S. No.	Technique	Key specification	Refs.	Integrating basin material	Results of yield
40	Transportable hemispherical solar still	Aluminium plate area = 0.5 m^2	[40]	Normal	2.8–5.7 l/m^2 d
41	Solar still	Basin area = 0.4 × 0.6 m^2	[41]	5-mm diffusion gaps	15.4 kg^{-2} m^{-2} d^{-1}
42	Tubular solar still	Length of trough = 0.49 m, Diameter of trough = 0.10 m	[42]	(1) Vinyl chloride sheet	(1) 0.5 kg/d
				(2) Polythene film	(2) 0.45 kg/d
43	Inverted trickle solar still	Basin area = 1 m^2, slope = 47°–17°	[43]	Intermediate headers	7.92 l/d
44	Solar still	Basin area = 0.25 m^2, slope = 15°, glass cover of 3-mm thickness	[44]	Floating-perforated black plate	(1) 15% (at brine depth of 3 cm)
					(2) 40% (at brine depth of 6 cm)
45	Non-conventional solar stills	Basin area = 1 m long, 0.5 m wide, 0.1 m high. Slope = 20°, glass cover of 3-mm thickness	[45]	Charcoal bed	15% increase in productivity
46	Continuous single-stage solar still	Basin area = 1 m^2, slope = 40°	[46]	Phase change energy storage mixture	4.536 L/m^2
47	Solar still	Basin area = 1 m^2, slope = 11°	[47]	Solar water heater	77% increase in productivity

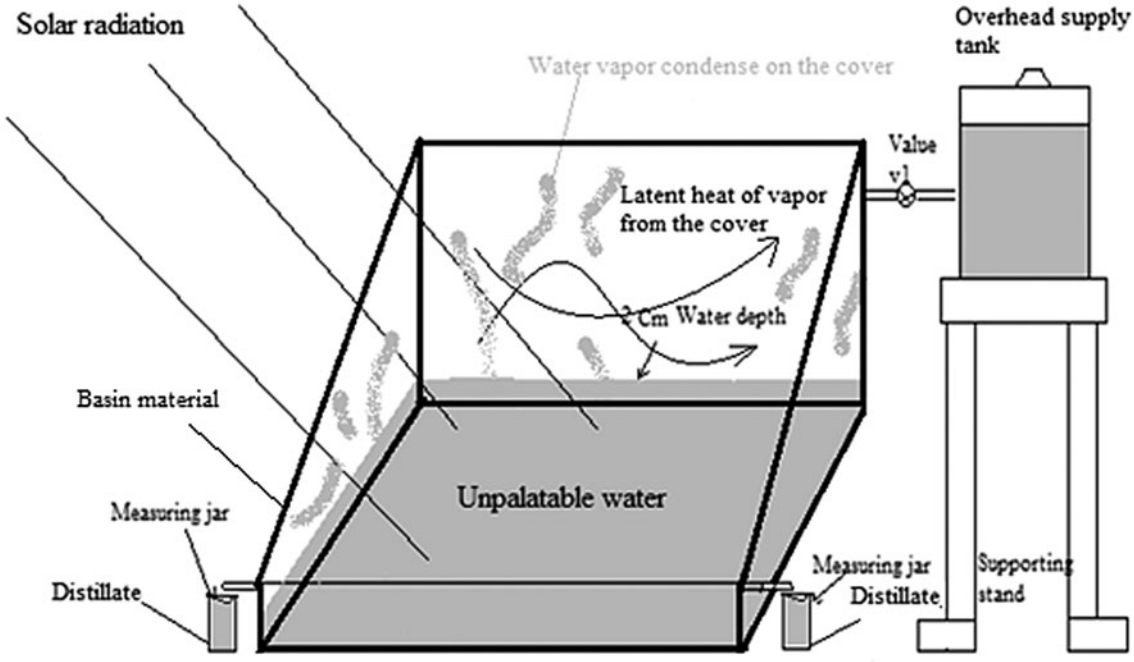

Fig. 1. Skeleton representation of the conventional solar still for the recovery of freshwater from the unpalatable water.

Table 2
Based on the latitude of the given area, tilt angle optimized is taken from Ref. [5]

S. No.	Latitude	Tilt angle
1	$\Phi \leq 14$ N or 14°S	$\beta = 14^{\circ}$
2	14°N ≤ Φ or 53°S	$6^{\circ} < \beta < 26^{\circ}$
3	15°S ≤ Φ or 55°S	$7.5^{\circ} < \beta < 26^{\circ}$

2.1. Glass solar still

An experimental investigation was carried out on glass basin solar still, with minimum saline water depth of 2 cm in the basin on a clear day (2 March 2014). The thermophysical properties of glass basin materials are taken from Table 3. Photograph of the glass basin solar still is shown in Fig. 2. During the daytime in the still, a higher heat transfer rate occurs and water productivity shows a higher variation in water production. The T_{atm} (°C), the T_{basin} (°C), the T_{water} (°C), daytime productivity increased in the glass basin solar still at 12.30 pm due to higher solar radiation 870 W/m^2 and low wind speed of 0.2 m/s as shown in Figs. 3 and 4, respectively. The basin and glass temperature difference is high for the high wind speed 0.4 m/s occuring between 3:00 and 05:00 pm which has a lower productivity. The freshwater productivity is 600 ml/m^2/d for the glass basin solar still.

2.2. Galvanized iron basin solar still

An experimental investigation was carried out on galvanized iron (GI) basin solar still, with minimum saline water depth of 2 cm in the basin on a clear day (17 March 2014). The thermophysical properties of GI basin materials are taken from Table 3. Photograph of a GI basin solar still is shown in Fig. 5. The T_{atm} (°C),

Table 3
Thermophysical properties of basin materials used in the experiment

Material	Density ρ (Kg/m^3)	Thermal diffusivity α (m^2/s)	Specific heat c (J/kg k)	Thermal conductivity (k W/m K)
Aluminium	2,707	84.18×10^{-6}	898	204.2
Galvanized iron	7,897	20.34×10^{-6}	452	72.7
Glass	2,500	7.46×10^{-7}	750	1.4

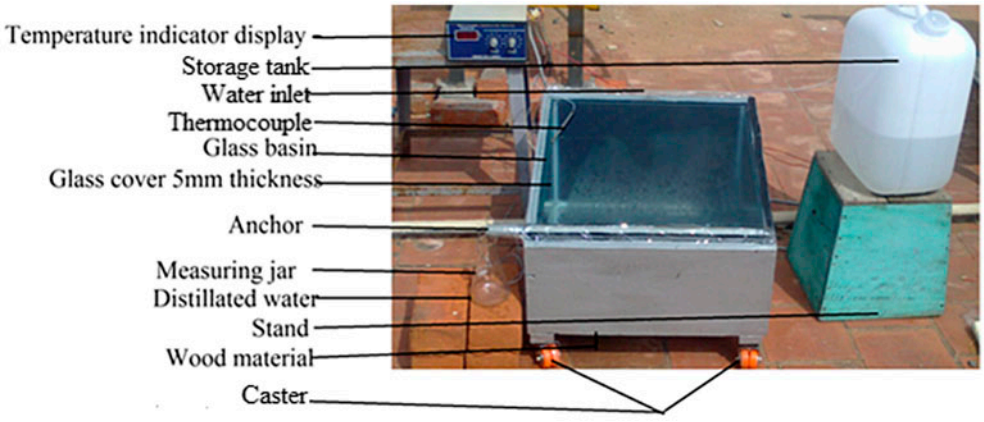

Fig. 2. Photograph of a glass basin solar still.

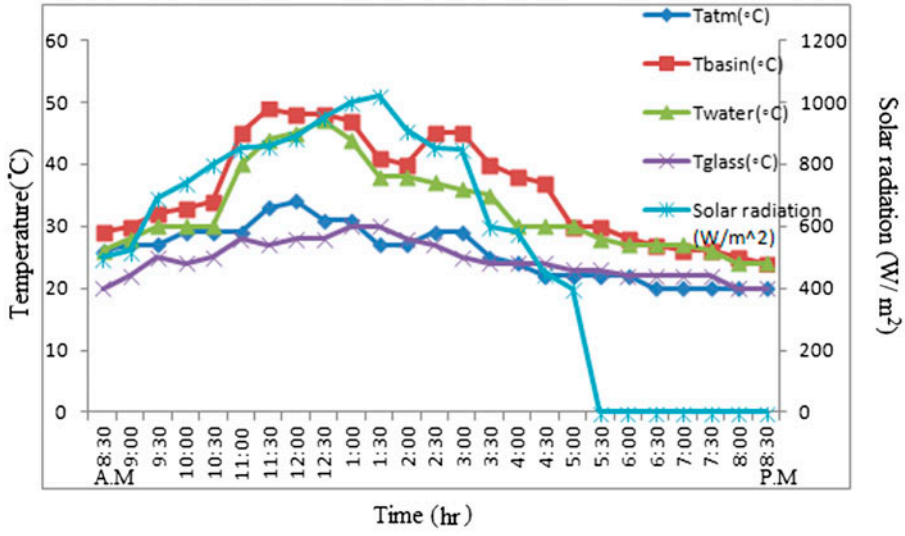

Fig. 3. Variation of time (h) with solar radiation (W/m^2) and the T_{atm} (°C), the T_{basin} (°C), the T_{water} (°C), the T_{glass} (°C) of the G solar still.

the T_{basin} (°C), the T_{water} (°C), daytime productivity increased in the GI basin solar still at 12.30 am by 1,031 W/m^2 due to higher solar radiation and low wind speed of 0.2 m/s, as shown in Figs. 6 and 7, respectively. The GI basin acts as an energy storage material which absorbs the heat during the morning and releases the heat during night (6.30–8.30 pm) which increases the productivity as shown in Fig. 7. The overall productivity of the GI basin solar still is higher than the glass basin solar still. For the high wind speed of 0.6 m/s, occurs between 6:00 and 7:30 pm which has the lower productivity. The fresh-water productivity is 1,000 ml/m^2/d for the GI basin solar still.

2.3. Aluminium solar still

An experimental investigation was carried out on aluminium basin solar still, with minimum saline water depth of 2 cm in the basin on a clear day (24 March 2014). The thermophysical properties of aluminium basin materials are taken from Table 3. Photograph of an aluminium basin solar still is shown in Fig. 8. The T_{atm} (°C), the T_{basin} (°C), the T_{water} (°C), daytime productivity increased in the glass basin solar still at 12.30 pm due to the higher solar radiation (951 W/m^2) and low wind speed of 0.2 m/s, as shown in Figs. 9 and 10, respectively. The aluminium basin acts as energy storage material which absorbs the heat

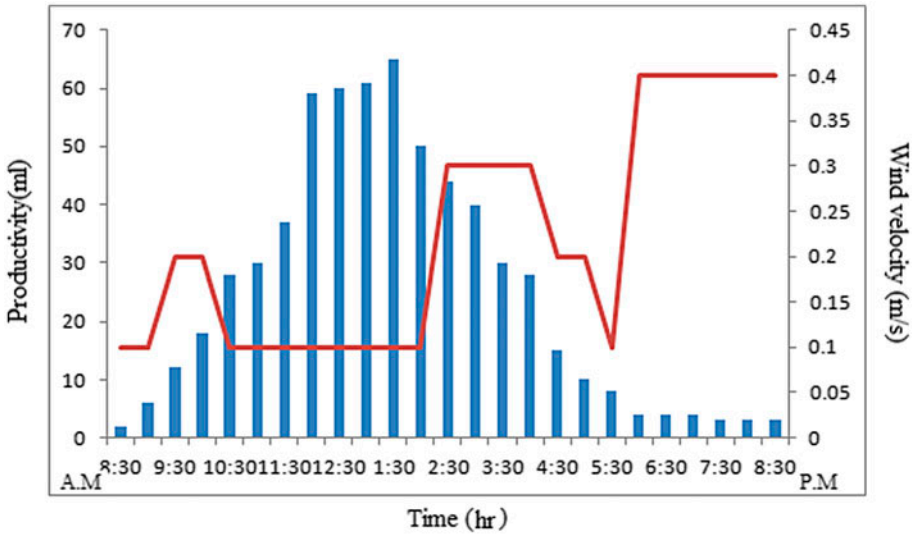

Fig. 4. Variation of time (h) with productivity (ml), wind velocity (m/s) of the G solar still.

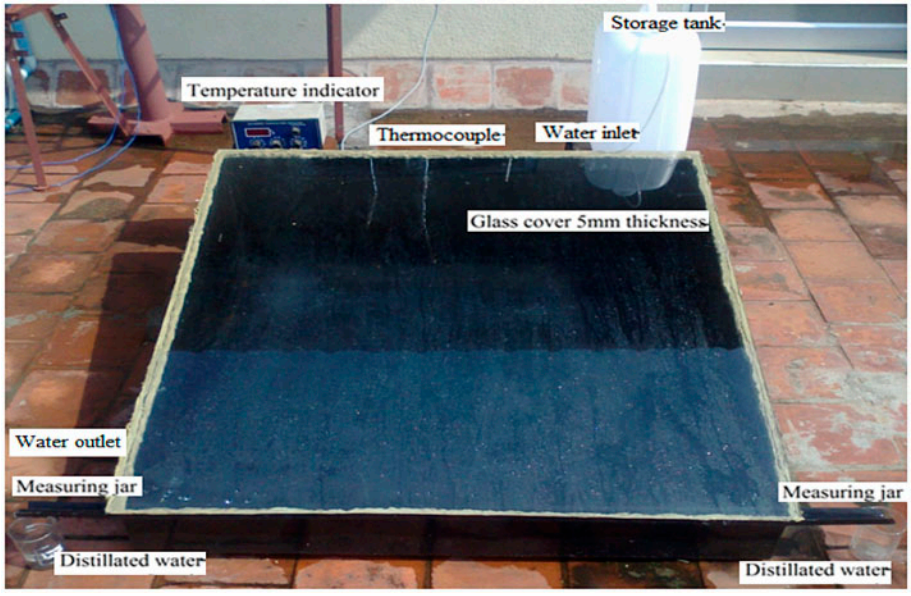

Fig. 5. Photograph of a GI basin solar still.

during the morning time and releases the heat during night time (6.30–8.30 pm) which increases the productivity, as shown in Fig. 10. The high wind speed of 0.4 m/s, occurs between 2:30 and 7:30 pm which has the lower productivity. The overall productivity of the aluminium basin solar still is higher than the GI basin solar still. The aluminium basin solar still has the highest distillate productivity of 2,000 ml/m^2/d compared to the glass basin and GI basin productivity.

3. Uncertainties analysis calculation

The following are the instruments used for the research work.

3.1. Thermocouple

The temperatures of the basin, glass, ambient and water were recorded with the help of K-type

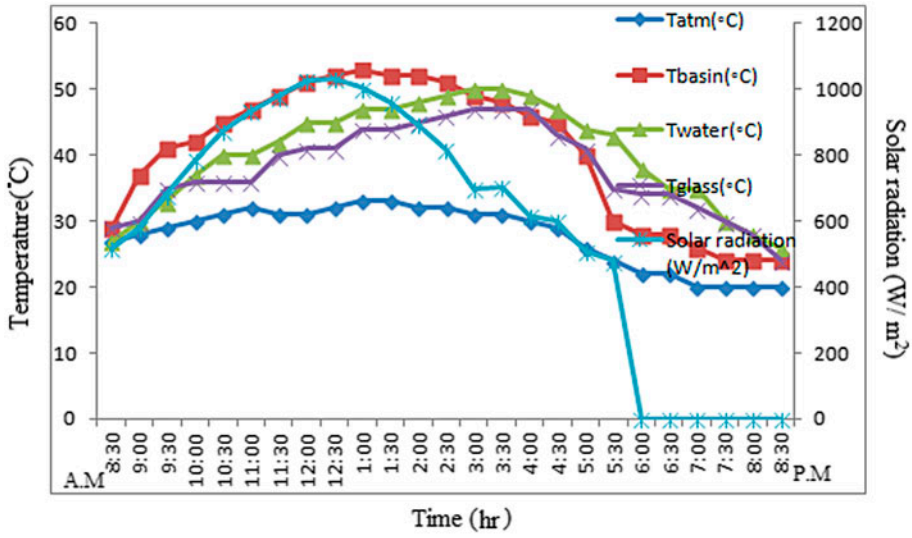

Fig. 6. Variation of time (h) with, solar radiation (W/m^2) and the T_{atm} (°C), the T_{basin} (°C), the T_{water} (°C), the T_{glass} (°C) of the GI solar still.

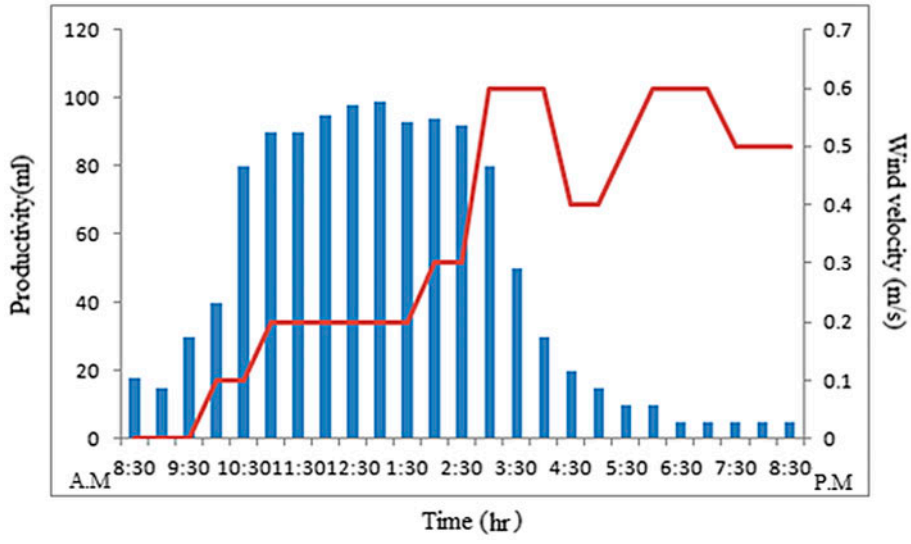

Fig. 7. Variation of time (h) with productivity (ml), wind velocity (m/s) of the GI solar still.

thermocouples and it has a range of 0–100°C. The accuracy of the the K-type thermocouples is ±0.1°C. Least experimental value is 15°C. Paramount possible error is 0.001. Percentage error for K-type thermocouples used in the experiment is 0.1%.

3.2. Solarimeter

The solarimeter is used to measure the solar intensity and it has a range of 0–5,000 W/m^2. The accuracy of the solarimeter is ±1 W/m^2. Least experimental value is 80 W/m^2. Paramount possible error is 0.0125. Percentage error for solarimeter used in the experiment is 1.25%.

3.3. Anemometer

The velocity of ambient air was measured with an anemometer and it has a range of 0–15 m/s. The accuracy of the anemometer is ±0.2 m/s. Least

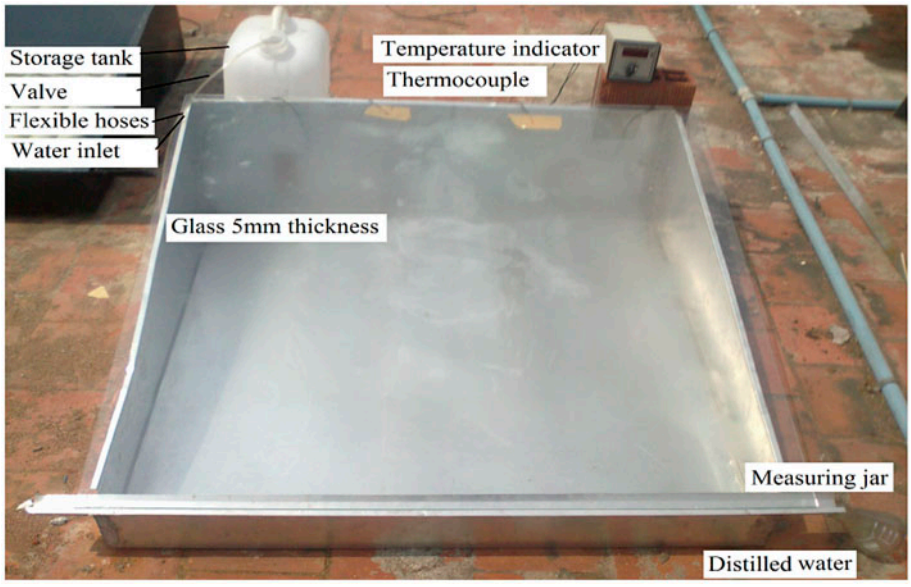

Fig. 8. Photograph of an aluminium basin solar still.

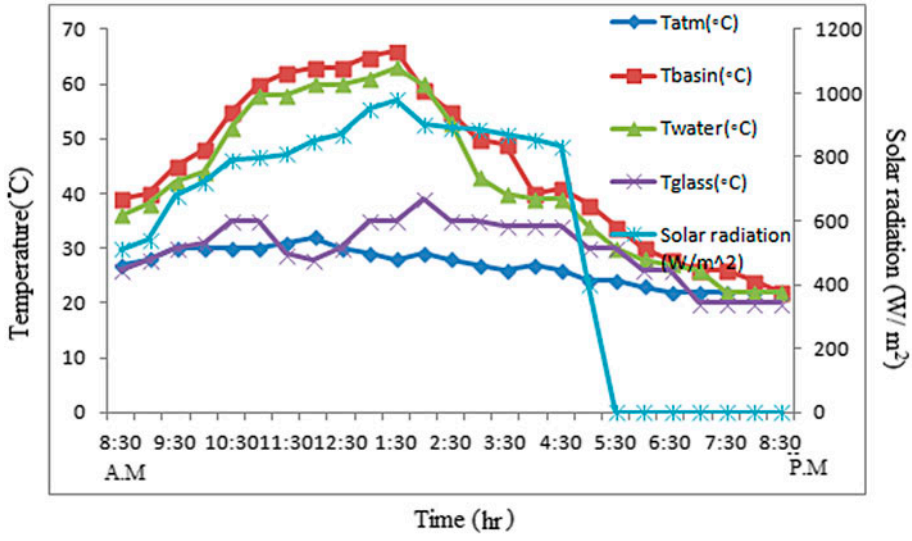

Fig. 9. Variation of time (h) with solar radiation (W/m^2) and the T_{atm} (°C), the T_{basin} (°C), the T_{water} (°C), the T_{glass} (°C) of the Al solar still.

experimental value is 1 m/s. Paramount possible error is 0.2. Percentage error for anemometer used in the experiment is 20%.

3.4. Collection tank

The collection tank is used to measure the productivity and it has a range of 0–1,000 ml. The accuracy of the collection tank is ±5 ml. Least experimental value is 100 ml. Paramount possible error is 0.05. Percentage error for collection tank used in the experiment is 5%.

4. Numerical investigations

The following section discusses the numerical investigations of the solar stills.

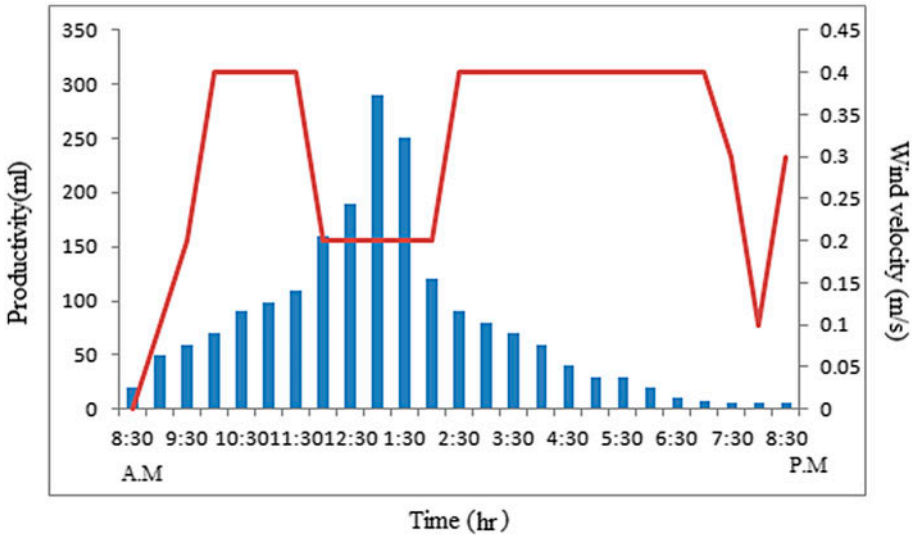

Fig. 10. Variation of time (h) with productivity (ml), wind velocity (m/s) of the Al solar still.

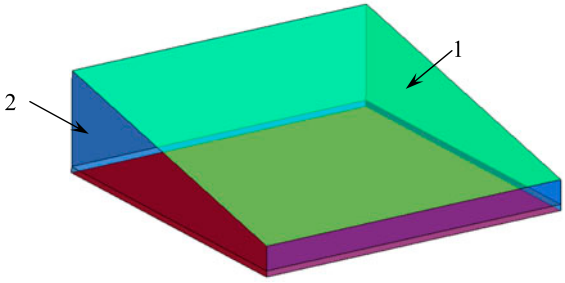

Fig. 11. Schematic sketch of the computational domain presently studied.
Notes: (1) Top cover: glass and (2) Bottom sheet: chosen material.

4.1. Computational model

The computational model is the volume of the fluid where the flow, heat and phase transfer interactions take place in the experimentally tested physical domain. Thus, the computational domain for the presently carried out numerical computations will be the internal volume of the solar still, which is the 'fluid domain'. The solid thickness of the plates/glass sheets used for the construction of the solar still was not considered for the numerical simulations. The schematic sketch of the computational domain considered for the present numerical simulation is shown in Figs. 11 and 12, respectively.

4.2. Governing equations

The following section discusses the governing equations used by the CFX solver for the generic flow and heat transfer problems. The governing equations for the multiphase flow problems are discussed in the subsequent section.

4.3. Generic flow and heat transfer problems

The fundamental governing equations for flow and heat transfer are the continuity, momentum (Navier–Stokes) and energy equations along with the equations for modelling the turbulence quantities. The governing equations are discussed in detail in this section. Based on the geometry and the phase transfer physics occurring in a solar still, the anticipated Rayleigh numbers will be well below the critical value and hence the flow can be treated as laminar in the present computations. The conservation equations for laminar flow in an inertial (non-accelerating) reference frame are presented here. The equation for conservation of mass, or continuity equation, can be written as follows:

$$\partial\rho/\partial t + \nabla \cdot (\rho\vec{v}) = S_{\mathrm{m}} \tag{1}$$

Eq. (1) is the general form of the mass conservation equation and is valid for incompressible as well as compressible flows. The source S_{m} is the mass added

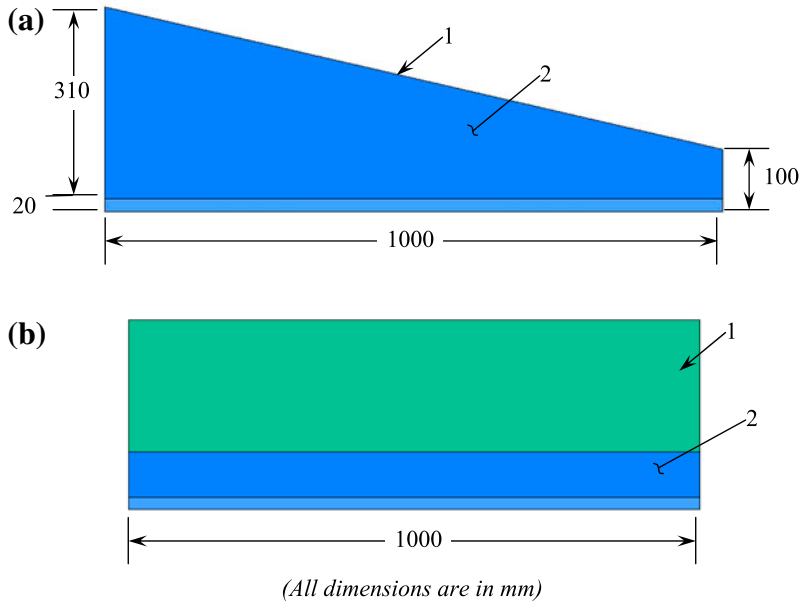

Fig. 12. Dimensions of the computational domain: (a) side view and (b) front view.

to the continuous phase from the dispersed second phase and any user-defined sources. The equation for the conservation of momentum in an inertial reference frame is given as:

$$(\rho\vec{v}) + \nabla \cdot (\rho\vec{v}\vec{v}) = -\nabla p + \nabla \cdot (\bar{\bar{\tau}}) + \rho\vec{g} + \vec{F} \tag{2}$$

where p is the static pressure, $\bar{\bar{\tau}}$ is the stress tensor, and $\rho\vec{g}$ and $\vec{F}$ are the gravitational body force and external body forces (e.g. that arise from interaction with the dispersed phase), respectively. $\vec{F}$ also contains other model-dependent source terms such as porous-media and user-defined sources. In the present computational study, only gravitational body force is included. The stress tensor $\bar{\bar{\tau}}$ is given by:

$$\bar{\bar{\tau}} = \mu\left[(\nabla\vec{v} + \nabla\vec{v}^T) - \frac{2}{3}\nabla \cdot \vec{v}I\right] \tag{3}$$

where μ is the molecular viscosity, I is the unit tensor and the second term on the right-hand side is the effect of volume dilation.

The CFD code solves the energy equation in the following form:

$$\partial/\partial t(\rho E) + \nabla \cdot (\vec{v}(\rho E + p)) = \nabla \cdot \left(k_{\text{eff}}\nabla T - \sum_j h_j\vec{J}_J + (\bar{\bar{\tau}}_{\text{eff}} \cdot \vec{v})\right) + S_h \tag{4}$$

where k_{eff} is the effective conductivity (= $k + k_t$, where k_t is the turbulent thermal conductivity, defined according to the turbulence model being used), h is the sensible enthalpy for ideal gases and $\vec{J}_j$ the diffusion flux of species j. The first three terms on the right-hand side of the equation represent energy transfer due to conduction, species diffusion and viscous dissipation, respectively.

4.4. Multiphase flow and heat transfer problems

Two distinct multiphase flow models are available in CFX:

(1) Eulerian–Eulerian multiphase model and
(2) Lagrangian particle tracking multiphase model.

This section describes Eulerian–Eulerian multiphase flow theory as used in the CFD solver CFX. This approach is valid for all types of flow where different phases of the fluid occupy the same control volume. Different phases of fluids are denoted using lowercase Greek letters α, β, γ etc. In general, a quantity subscribed with α, β, γ etc. refers to the value of the quantity for that particular phase. For example, the volume fraction of α is denoted as r_α. Thus, the volume V_α occupied by phase α in a small volume V around a point of volume fraction r_α is given by:

$$V_\alpha = r_\alpha \cdot V \tag{5}$$

This is the actual mass per unit volume of phase α, given that phase α only occupies a fraction of the volume, that is the mass of α, per unit volume of the bulk fluid.

The mixture density is given by:

$$\rho_{\mathrm{m}} = \sum_{\alpha} \rho_{\alpha} r_{\alpha} \tag{6}$$

Interfacial transfer of momentum, heat and mass is directly dependent on the contact surface area between the two phases. This is characterized by the interfacial area per unit volume between phase α and phase β, known as the interfacial area density $A_{\alpha\beta}$. Note that it has dimensions of inverse length. Interfacial transfer can be modelled using either the particle or mixture models. These essentially provide different algebraic prescriptions for the interfacial area density.

4.5. Continuity equation

The continuity equation for the homogeneous multiphase flow is described below:

$$\frac{\partial}{\partial t}(r_{\alpha}.\rho_{\alpha}) + \nabla.(r_{\alpha}\rho_{\alpha}U_{\alpha}) = S_{\mathrm{MS}\alpha} + \sum_{\beta=1}^{N_P} \Gamma\alpha\beta \tag{7}$$

where $S_{\mathrm{MS}\alpha}$ describes user-specified mass sources. $\Gamma\alpha\beta$ is the mass flow rate per unit volume from phase β to phase α. This term only occurs if interphase mass transfer takes place.

4.6. Momentum equation

The momentum equation for the homogeneous multiphase flow is given below:

$$\frac{\partial}{\partial t}(\rho U) + \nabla.\left(\rho U \otimes U - \mu\left(\nabla U + (\nabla U)^{T}\right)\right) = S_{\mathrm{M}} - \nabla p \tag{8}$$

where

$$\rho = \sum_{\alpha=1}^{N_P} r_{\alpha} \cdot \rho_{\alpha} \text{ and } \mu = \sum_{\alpha=1}^{N_P} r_{\alpha} \cdot \mu_{\alpha}$$

4.7. Interphase momentum transfer

When using the homogeneous model, momentum transfer between phases is assumed to be very large. Interphase momentum transfer, $M_{\alpha\beta}$, occurs due to interfacial forces acting on each phase α, due to interaction with another phase β. The total force on phase α due to interaction with other phases is denoted as M_{α}, and is given by:

$$M_{\alpha} = \sum_{\beta \neq \alpha} M_{\alpha\beta} \tag{9}$$

Note that interfacial forces between two phases are equal and opposite, so the net interfacial forces sum to zero:

$$M_{\alpha\beta} = -M_{\beta\alpha} \Rightarrow \sum_{\alpha} M_{\alpha} = 0 \tag{10}$$

The total interfacial force acting between two phases may arise from several independent physical effects:

$$M_{\alpha\beta} = M_{\alpha\beta}^{\mathrm{D}} + M_{\alpha\beta}^{\mathrm{L}} + M_{\alpha\beta}^{\mathrm{LUB}} + M_{\alpha\beta}^{\mathrm{VM}} + M_{\alpha\beta}^{\mathrm{TD}} + M_{\mathrm{S}} + \ldots \tag{11}$$

The forces indicated above, respectively, represent the interphase drag force, lift force, wall lubrication force, virtual mass force, turbulence dispersion force and solids pressure force (for dense solid particle phases only).

4.8. Conservation equations

Other than the governing equations, the following conservation equations are needed to arrive at the proper solution.

4.9. Volumetric conservation

The volumetric constraint tells that the sum of the volume fractions of the phases considered in the study should sum to unity:

$$r_{\alpha} + r_{\beta} = 1 \tag{12}$$

4.10. Pressure constraint

This condition ensures that all the phases in the mixture share the same pressure field in the computational domain:

$$P_{\alpha} = P_{\beta} = P \tag{13}$$

Table 4
Thermal boundary conditions for CFD analysis

Basin material	Temperature (°C) @ 12:30 PM				Solar radiation (W/m^2)
	Ambient	Basin	Water	Glass	
Al	30	63	60	30	870
GI	32	52	53	52	1,031
G	31	48	47	28	951

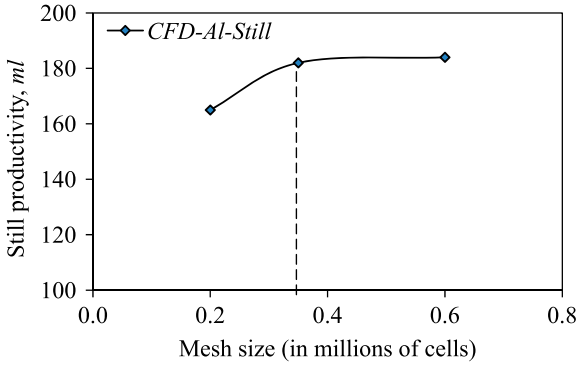

Fig. 13. Variation of solar still productivity with different mesh densities.

4.11. Interphase mass transfer

Interphase mass transfer occurs when mass is carried from one phase into another. It is applicable to both the inhomogeneous and homogeneous multiphase models. Mass transfer is represented by sources in the phase continuity Eq. (7). As interfacial area is commonly proportional to volume fraction, this permits automatic linearization of mass transfer terms relative to volume fraction.

4.12. Boundary conditions

For any thermal CFD analysis, an appropriate thermal boundary condition is important for an accurate prediction. The thermal energy gain of the absorber fluid, to affect the phase transfer, depends mainly on the incident heat flux. For the present numerical analysis, isothermal boundary conditions identified from the experiments at a chosen time of the day, say 12:30 PM, data were used and chosen from Figs. 3, 6, and 9. Experimentally measured absorber plate temperature i.e. basin temperature at the bottom and the steam condensing glass temperature at the top were used as the boundary conditions.

Table 4 shows the thermal boundary conditions used for the present CFD analysis, with inputs from the present experiments. The temperature values of ambient, basin material, water and glass temperature estimated at 12:30 PM are tabulated. The corresponding solar insolation as estimated from the experiments is also shown in the last column of the Table 4.

4.13. Discretization

Meshing was carried out using the preprocessing tool Gambit 2.4 to generate hex-dominant finite-volume elements throughout the computational domain. Finer near wall meshing is developed using the boundary layer mesh feature of the preprocessor with the first node at 0.1 mm and with a default growth factor of 1.1 for 10 layers. This is done to capture the flow and thermal features happening close to the wall more accurately.

4.14. Grid independency

Grid independency tests are carried out for the solar still with the quantity of freshwater generated or the productivity of the still as the assessment criteria. Fig. 13 shows the variation of productivity in the solar still with aluminium as the absorber basin material with different mesh densities. It can be observed that the productivity increases from a mesh size of 2.0 to 3.5 million cells. The variation of the productivity from 3.5 to 6.0 million cells is very less, which indicates that the effect of mesh density is insignificant beyond 3.5 million cells and hence it was decided to continue with the mesh settings of 3.5 million cells for the present study. Fig. 14(a) shows the isometric view of the computational domain mesh that was used for the present study, whereas Fig. 14(b) shows the side view of the mesh. A total of 35 elements were used in the still height direction and 100 elements in the still length and breadth directions.

4.15. Numerical details

The computations were carried out as a steady, incompressible, three-dimensional Reynolds-averaged Navier–Stokes (RANS) solution with VOF approach

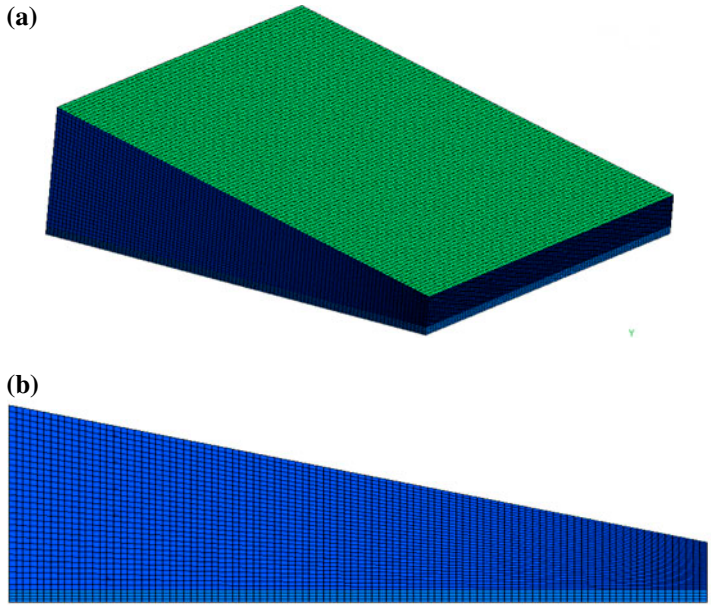

Fig. 14. Details of the meshed computational domain: (a) isometric view and (b) side view.

for the phase changing interaction between water and water vapour. Two-phase approach was used with water vapour as the primary phase and liquid water as the secondary phase. A water depth of 2 cm used in the experiments was specified as the initial condition in the simulations by patching the liquid volume defined in the preprocessor with a secondary phase volume fraction value of 1. The vapour volume defined earlier was patched with a corresponding value of 0.

Gravity option was enabled to include the natural gravitational pull for the condensing vapour into fresh liquid water to fall down. For the evaporating vapour to rise up due to buoyancy effect, an appropriate option was enabled in the property definition for the vapour material. A user-defined function (UDF) was developed to make the phase transfer between liquid water and water vapour. The UDF was compiled inside the Ansys Fluent solver and hooked to the solver as a UDF in the mass transfer interaction panel. The UDF can be found in Appendix 1.

Simple scheme was used to couple the pressure and velocity and second-order up-winding scheme for the spatial discretization of most of the governing terms. For the volume of fluid alone, first-order up-winding was chosen to control the solution convergence. Default values of under-relaxation were used for all the solution control terms. To make the solution stable, initial 100 iterations were carried out by disabling the phase transfer physics.

4.16. Convergence criteria

The convergence criteria for the computational solution are determined based on scaled residuals for the equations of continuity, momentum equations and phase transfer parameter such as the volume fraction of the secondary phase fluid. The scaled residuals for solution convergence are set to 10^{-5} for all governing equations. The solution is considered to be converged when all the scaled residuals are less than or equal to this prescribed value. Computations are carried out until the steady state is reached.

4.17. Results and discussion

The results from the computational analysis with three different solar still basin materials, aluminium (Al), GI and glass (G) are discussed in this section. A comparison of the numerically estimated productivity of the solar still is compared with that of the experiments.

4.18. Basin material—aluminium (Al)

Fig. 15 shows the contours of liquid volume fraction in the solar still with Al as the basin material. The corresponding thermal boundary conditions applied to the CFD, from the experiments, can be found in Table 4. Fig. 15(a) shows the contours of liquid fraction at the bottom of the still, at the start of

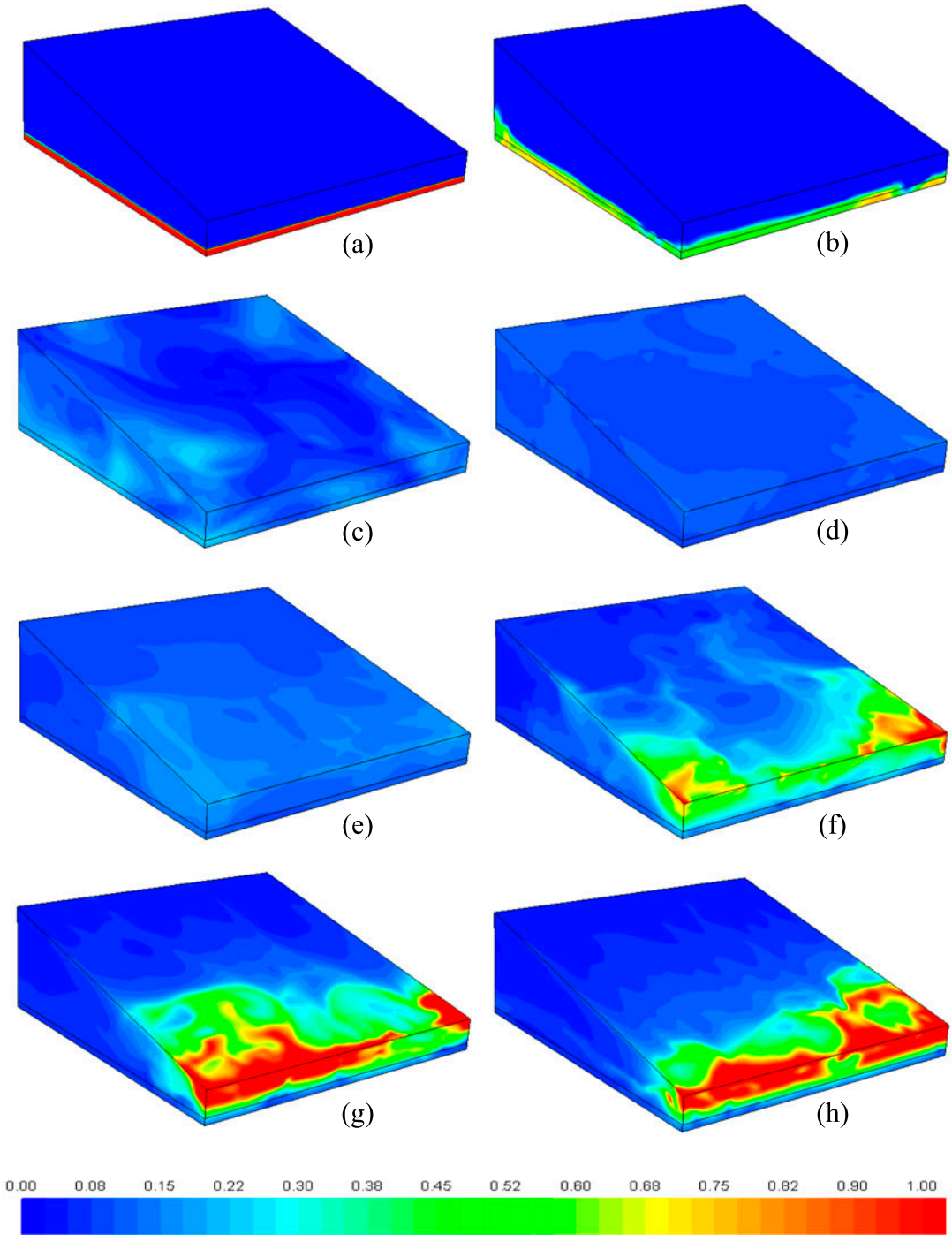

Fig. 15. Contours of liquid water fraction—Al still.

the simulations, indicating that the still was initiated with a fixed water level. With rise in temperature of water in the still, phase change occurs within the still and the steam is produced. This change in phase can be observed in Fig. 15(b)–(e), which can be visualized from the decreased volume fraction of the secondary phase fluid i.e. liquid water.

Due to buoyancy, the steam thus produced rises up and when the steam is in contact with the glass surface at the top, the steam starts condensing and

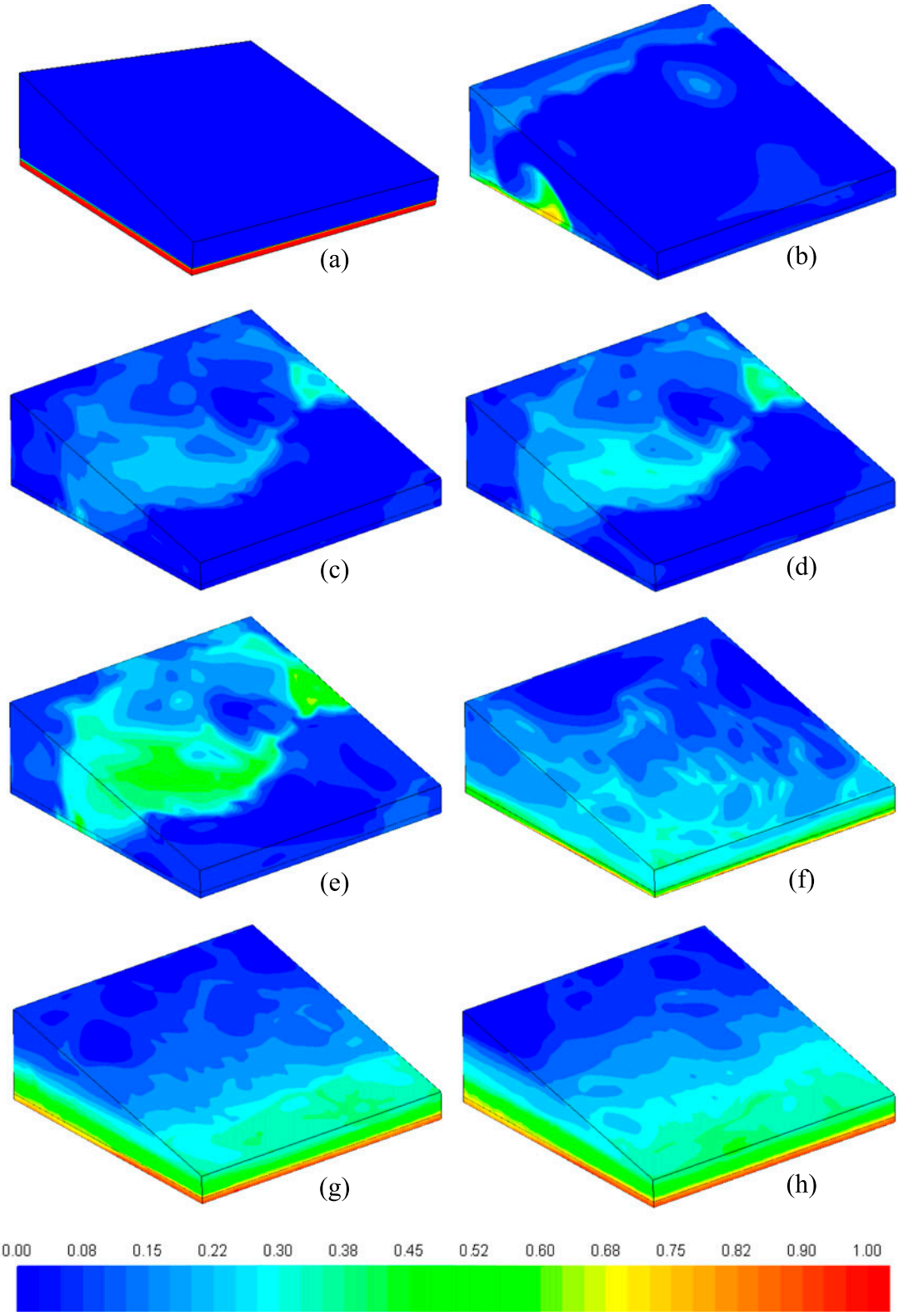

Fig. 16. Contours of liquid water fraction—GI still.

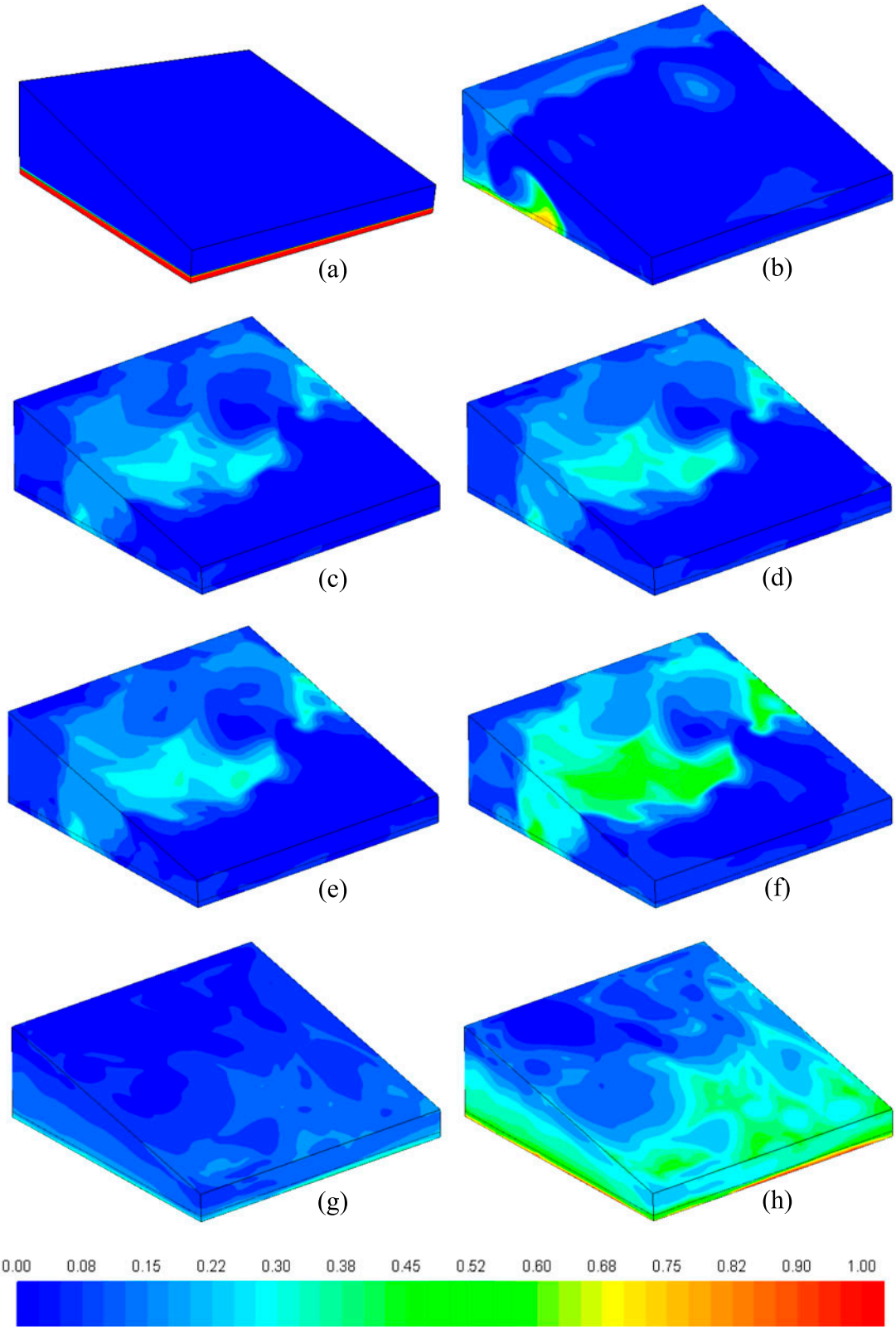

Fig. 17. Contours of liquid water fraction—G still.

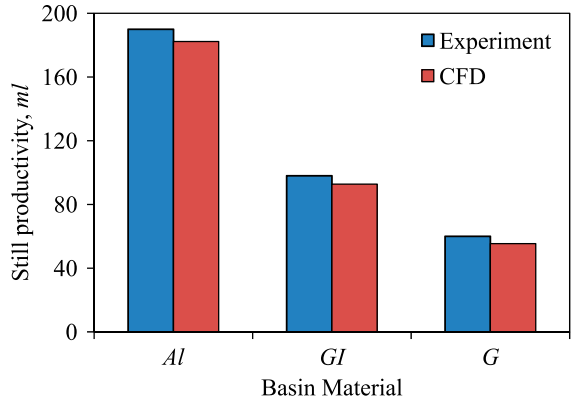

Fig. 18. Comparison of present experimental and CFD results.

produces freshwater. Fig. 15(f)–(h) show the freshwater condensation which can be seen from the increased volume fraction of the secondary phase. The freshwater production rate was continuously monitored and the total freshwater produced for 30 min was estimated. The freshwater production from the CFD analysis was found to be 182.3 ml.

4.19. Basin material—GI

Figs. 5 and 6 show the contours of liquid volume fraction in the solar still with GI as the basin material. Similar to the Al still, with rise in temperature of water in the still, phase change occurs within the still and steam is produced. This change in phase can be observed in Fig. 16(b)–(e), which can be visualized from the decreased volume fraction of the secondary phase fluid i.e. liquid water. Fig. 16(f)–(h) shows the freshwater condensation which can be seen from the increased volume fraction of the secondary phase. The freshwater production rate was continuously monitored and the total freshwater produced for 30 min was estimated. The freshwater production from the CFD analysis was found to be 92.8 ml. Compared to the Al basin material, the GI basin material gave a lesser productivity.

4.20. Basin material—glass (G)

Fig. 17 shows the contours of liquid volume fraction in the solar still with G as the basin material. Similar to the Al still, with rise in temperature of water in the still, phase change occurs within the still and steam is produced. This change in phase can be observed in Fig. 17(b)–(e), which can be visualized from the decreased volume fraction of the secondary phase fluid i.e. liquid water. Fig. 17(f)–(h) shows the freshwater condensation which can be seen from the increased volume fraction of the secondary phase. The freshwater production rate was continuously monitored and the total freshwater produced for 30 min was estimated. The freshwater production from the CFD analysis was found to be 55.4 ml. Compared to the Al and GI basin materials, the G basin material gave a lesser productivity.

5. An economic analysis of the solar stills

5.1. An economic analysis calculation for the glass solar still

The total fixed cost of the glass solar still includes the sum of the insulation, the basin material, the paint, the flexible hoses, a valve and the auxiliary system. The total fixed cost of the plastic solar still is $F = 5$ \$. The total cost of the glass solar still C is equal to the sum of the fixed cost and the variable cost. Assuming that the variable cost V equals $0.3\,F$ per year [5] and the expected still life is 10 years, then $C = 5 + (0.3 \times 5 \times 10) = 20$ \$. The minimum average productivity of the solar still is 600 ml/m^2/d from the experimental result. Chennai is a suitable hot place, where the solar still can operate for 335 d. The total productivity of the solar still lifetime = 600 ml × 10 × 335 = 2,010 L. The cost of one litre of water from the glass solar still = 20/2,010 = 0.001 \$.

5.2. An economic analysis calculation for the GI solar still

The total fixed cost of the GI solar still includes the sum of the insulation, the basin material, the paint, the flexible hoses, a valve and the auxiliary system. The total fixed cost of the conventional solar still is $F = 25$ \$. The total cost of the GI solar still C is equal to the sum of the fixed cost and the variable cost. Assuming that the variable cost V equals 0.3 F per year [5] and the expected still life is 10 years, then $C = 100 + (0.3 \times 100 \times 10) = 400$ \$. The minimum average productivity of the solar still is 1,000 ml/m^2/d from the experimental result. Chennai is a suitable hot place, where the solar still can operate for 335 d. The total productivity of the solar still lifetime = 1 × 10 × 335 = 3,350 L. The cost of one litre of water from the GI solar still = 100/3,350 = 0.029 \$.

5.3. An economic analysis calculation for the aluminium solar still

The total fixed cost of the aluminium solar still $F = 90$ \$. The total cost of the solar still C is equal to the sum of the fixed cost and the variable cost.

Assuming that the variable cost V equals 0.3 F per year [5] and the expected still life is 10 years, then $C = 90 + (0.3 \times 90 \times 10) = 360$ \$. The minimum average productivity of the solar still is 2,000 ml/m^2/d from the experimental result. Assume that the solar still can operate for 335 d. The total productivity of the solar still lifetime = 2 × 10 × 335 = 6,700 L. The cost of one litre of water from the aluminium solar still = 360/6,700 = 0.055 \$.

6. Conclusion

The comparisons of the present experimental and present computational results for the same boundary conditions in CFD as that of experiment are shown in Fig. 18. The results showed that the solar still with Al basin material was found to show the highest freshwater production. The GI basin material followed next to Al and the least freshwater generation was observed in G basin material. Overall observation showed that the present CFD results are in good agreement with the experimental values. This validates the presently adopted computational methodology.

References

[1] P. Malaiyappan, N. Elumalai, Design, fabrication and performance analysis of single basin solar stills, Appl. Mech. Mater. 372 (2013) 590–593.
[2] P. Malaiyappan, N. Elumalai, Review of the productivity of various types of solar stills, Desalin. Water Treat. 54(12) (2015) 3236–3247.
[3] T. Elango, K. Kalidasa Murugavel, The effect of the water depth on the productivity for single and double basin double slope glass solar stills, Desalination 359 (2015) 82–91.
[4] G. Singh, S. Kumar, G.N. Tiwari, Design, fabrication and performance evaluation of a hybrid photovoltaic thermal (PVT) double slope active solar still, Desalination 277 (2011) 399–406.
[5] P. Malaiyappan, N. Elumalai, Productivity enhancement of a single-basin and single-slope solar still coupled with various basin materials, Desalin. Water Treat. (2015) 1–15, doi: 10.1080/19443994.2014.1003973.
[6] Z.M. Omara, A.E. Kabeel, The performance of different sand beds solar stills, Int. J. Green Energy 11 (2014) 240–254.
[7] V. Velmurugan, C.K. Deenadayalan, H. Vinod, K. Srithar, Desalination of effluent using fin type solar still, Energy 33 (2008) 1719–1727.
[8] K. Kalidasa Murugavel, S. Sivakumar, J. Riaz Ahamed, K.K.S.K. Chockalingam, K. Srithar, Single basin double slope solar still with minimum basin depth and energy storing materials, Appl. Energy 87 (2010) 514–523.
[9] T. Rajaseenivasan, P. Nelson Raja, K. Srithar, An experimental investigation on a solar still with an integrated flat plate collector, Desalination 347 (2014) 131–137.
[10] V.K. Dwivedi, G.N. Tiwari, Experimental validation of thermal model of a double slope active solar still under natural circulation mode, Desalination 250 (2010) 49–55.
[11] G. Mink, M.M. Aboabboud, É. Karmazsin, Air-blown solar still with heat recycling, Sol. Energy 62 (1998) 309–317.
[12] O.M. Haddad, M.A. Al-Nimr, A. Maqableh, Enhanced solar still performance using a radiative cooling system, Renewable Energy 21 (2000) 459–469.
[13] K. Fukuia, T. Nosoko, H. Tanaka, T. Nagata, A new maritime lifesaving multiple-effect solar still design, Desalination 160 (2004) 271–283.
[14] A.A. Madani, G.M. Zaki, Yield of solar stills with porous basins, Appl. Energy 52 (1995) 273–281.
[15] M. Reali, G. Modica, Solar stills made with tubes for sea water desalting, Desalination 220 (2008) 626–632.
[16] S. Toyama, K. Murase, Solar stills made from waste materials, Desalination 169 (2004) 61–67.
[17] A. Joyce, D. Loureiro, M. Collares Pereira, M. Moreira, A spray evaporation type solar still, Renewable Energy 5 (1994) 517–519.
[18] T. Arunkumar, R. Jayaprakash, A. Ahsan, D. Denkenberger, M.S. Okundamiya, Effect of water and air flow on concentric tubular solar water desalting system, Appl. Energy 103 (2013) 109–115.
[19] D.A. Balladin, O. Headley, A. Roach, Evaluation of a concrete cascade solar still, Renewable Energy 17 (1999) 191–206.
[20] A.A. Badran, A.A. A1-Hallaq, I.A.E. Salman, M.Z. Odat, A solar still augmented with a flat-plate collector, Desalination 172 (2005) 227–234.
[21] G.M. Cappelletti, An experiment with a plastic solar still, Desalination 142 (2002) 221–227.
[22] S. Kumar, A. Tiwari, Design, fabrication and performance of a hybrid photovoltaic/thermal (PV/T) active solar still, Energy Convers. Manage. 51 (2010) 1219–1229.
[23] B. Selva Kumar, S. Kumar, R. Jayaprakash, Performance analysis of a "V" type Solar using a charcoal absorber and a boosting mirror, Desalination 229 (2008) 217–230.
[24] Y. Taamneh, M.M. Taamneh, Performance of pyramid-shaped solar still: Experimental study, Desalination 291 (2012) 65–68.
[25] K. Murase, Y. Yamagishi, Y. Iwashita, K. Sugino, Development of a tube-type solar still equipped with heat accumulation for irrigation, Energy 33 (2008) 1711–1718.
[26] H. Aburideh, A. Deliou, B. Abbad, F. Alaoui, D. Tassalit, Z. Tigrine, An experimental study of a solar still: Application on the sea water desalination of Fouka, Procedia Eng. 33 (2012) 475–884.
[27] S. Jasrotia, A. Kansal, V.V.N. Kishore, Application of solar energy for water supply and sanitation in Arsenic affected rural areas: A study for Kaudikasa village, India, J. Cleaner Prod. 60 (2013) 102–106.
[28] D.A. Haralambopoulos, G. Biskos, C. Halvadakis, T.D. Lekkas, Dewatering of wastewater sludge through a solar still, Renewable Energy 26 (2002) 247–256.
[29] P.U. Suneesh, R. Jayaprakash, T. Arunkumar, D. Denkenberger, Effect of air flow on "V" type solar still with cotton gauze cooling, Desalination 337 (2014) 1–5.

[30] M.M. El-Kassaby, Parabolic type solar still, Renewable Energy 1 (1991) 449–454.
[31] Z.M. Omara, M.A. Eltawil, Hybrid of solar dish concentrator, new boiler and simple solar collector for brackish water desalination, Desalination 326 (2013) 62–68.
[32] P. Monowe, M. Masale, N. Nijegorodov, V. Vasilenko, A portable single-basin solar still with an external reflecting booster and an outside condenser, Desalination 280 (2011) 332–338.
[33] A.A. El-Sebaii, S. Aboul-Enein, E. El-Bialy, Single basin solar still with baffle suspended absorber, Energy Convers. Manage. 41 (2000) 661–675.
[34] R. Dev, G.N. Tiwari, Characteristic equation of the inverted absorber solar still, Desalination 269 (2011) 67–77.
[35] M.A. Eltawil, Z. Zhengming, Wind turbine-inclined still collector integration with solar still for brackish water desalination, Desalination 249 (2009) 490–497.
[36] A.M. El-Zahaby, A.E. Kabeel, A.I. Bakry, S.A. El-agouz, O.M. Hawam, Augmentation of solar still performance using flash evaporation, Desalination 257 (2010) 58–65.
[37] S. Abdallah, O.O. Badran, Sun tracking system for productivity enhancement of solar still, Desalination 220 (2008) 669–676.
[38] H. Tanaka, Y. Nakatake, A vertical multiple-effect diffusion-type solar still coupled with a heat-pipe solar collector, Desalination 160 (2004) 195–205.
[39] H. Zheng, Z. Chang, Z. Chen, G. Xie, H. Wang, Experimental investigation and performance analysis on a group of multi-effect tubular solar desalination devices, Desalination 311 (2013) 62–68.
[40] B.I. Ismail, Design and performance of a transportable hemispherical solar still, Renewable Energy 34 (2009) 145–150.
[41] H. Tanaka, T. Nosoko, T. Nagata, A highly productive basin-type-multiple-effect coupled solar still, Desalination 130 (2000) 279–293.
[42] A. Ahsan, Kh.M. Shafiul Islam, T. Fukuhara, A.H. Ghazali, Experimental study on evaporation, condensation and production of a new Tubular Solar Still, Desalination 260 (2010) 172–179.
[43] A.A. Badran, L.M. Assaf, K.S. Kayed, F.A. Ghaith, M.I. Hammash, Simulation and experimental study for an inverted trickle solar still, Desalination 164 (2004) 77–85.
[44] A. Safwat Nafey, M. Abdelkader, A. Abdelmotalip, A.A. Mabrouk, Enhancement of solar still productivity using floating perforated black plate, Energy Convers. Manage. 43 (2002) 937–946.
[45] M.M. Naim, M.A. Abd El Kawi, Non-conventional solar stills part 1. Non-conventional solar stills with charcoal particles as absorber medium, Desalination 153 (2002) 55–64.
[46] M.M. Naim, M.A. Abd El Kawi, Non-conventional solar stills part 2. Non- conventional solar stills with energy storage element, Desalination 153 (2002) 71–80.
[47] K. Sampathkumar, P. Senthilkumar, Utilization of solar water heater in a single basin solar still—An experimental study, Desalination 297 (2012) 8–19.

Appendix 1

UDF in the Mass Transfer Interaction Panel

```
#include "udf.h"
DEFINE_MASS_TRANSFER(liq_gas_source,cell,thread,
from_index,from_species_index,to_index,to_species_index)
{
real m_lg;
real T_SAT=312.25;
Thread*gas=THREAD_SUB_THREAD(thread,from_index);
Thread*liq=THREAD_SUB_THREAD(thread,to_index);
m_lg=0;
if(C_T(cell,liq)>=T_SAT)
{
m_lg =−0.1*C_VOF(cell,liq)*C_R(cell,liq)*fabs(C_T(cell,liq)-T_SAT)/T_SAT;
}
if((m_lg==0)&&(C_T(cell,gas)<=T_SAT))
{
m_lg=0.1*C_VOF(cell,gas)*C_R(cell,gas)*fabs(T_SAT-C_T(cell,gas))/T_SAT;
}
return (m_lg);
}
```